Acta Materialia 249 (2023) 118829

Contents lists available at ScienceDirect

Acta Materialia

journal homepage: www.elsevier.com/locate/actamat

Full length article

Room-temperature deformation of single crystals of the sigma-phase compound FeCr with the tetragonal $D8_b$ structure investigated by micropillar compression

Kyosuke Kishida [a,b,*], Masaomi Okutani [a], Hirotaka Suzuki [a], Haruyuki Inui [a,b], Martin Heilmaier [c], Dierk Raabe [d]

[a] Department of Materials Science and Engineering, Kyoto University, Sakyo-ku, Kyoto 606-8501, Japan
[b] Center for Elements Strategy Initiative for Structural Materials (ESISM), Kyoto University, Sakyo-ku, Kyoto 606-8501, Japan
[c] Institute for Applied Materials (IAM-WK), Karlsruhe Institute of Technology (KIT), Engelbert-Arnold-Strasse 4, 76131 Karlsruhe, Germany
[d] Department of Microstructure Physics and Alloy Design, Max-Planck-Institut für Eisenforschung, Düsseldorf, Germany

ARTICLE INFO

Keywords:
Sigma phase
Deformation structure
Dislocations
Zonal dislocations
Mechanical properties
Micropillar compression

ABSTRACT

The deformation behavior of single crystals of the sigma-phase compound FeCr with the tetragonal $D8_b$ structure has been investigated by micropillar compression at room temperature as a function of crystal orientation and specimen size. In spite of the repeatedly reported brittleness, plastic flow is observed at room temperature for all loading axis orientations tested. Three slip systems, {100}[001], {100}<010> and {111}<0$\bar{1}$1> are newly identified to be operative at room temperature depending on the loading axis, in addition to {110}[001] slip we previously identified. The CRSS values for all the identified slip systems are very high exceeding 1.3 GPa and decrease with increasing specimen size, following an inverse power-law relationship with a very small power-law exponent. Similarly to {110}[001] slip, {100}[001] slip is confirmed to be carried by the motion of [001] zonal dislocations through atomic-resolution scanning transmission electron microscopy imaging of their core structures. <010> dislocations gliding on {100} are confirmed to dissociate into two collinear partial dislocations, while <0$\bar{1}$1> dislocations gliding on {111} to dissociate into three collinear partial dislocations. The fracture toughness values estimated by micro-cantilever bend tests of chevron-notched micro beam specimens are indeed very low, 1.6~1.8 MPa·m$^{1/2}$ (notch plane // (001) and (100)), indicating significant brittleness of sigma FeCr.

1. Introduction

A series of sigma-phase compounds are of technological importance as they are known to precipitate in some high-temperature structural materials based on iron and nickel [1–7]. The intermetallic compound FeCr is the prototype of these sigma-phase compounds that have a complex primitive tetragonal structure of the $D8_b$ type (in the Strukturbericht symbol) with the space group of $P4_2/mnm$ (No.136) and the Pearson's symbol of $tP30$ [8]. The $D8_b$ structure of the sigma phase compound FeCr is composed of three different kinds of atomic layers designated as *A, B* and *C* stacked along the tetragonal *c*-axis with the stacking sequence of *ACBC* (Fig. 1(a)). Atomic layers *A* (at $z = 0$) and *B* (at $z = 1/2$) have an identical atomic arrangement of the Kagome-type and are related to each other by the 90°-rotation about the *c*-axis so as to generate 4_2 screw axes along the *c*-axis, while the atomic arrangement in Atomic layer *C* (at z ~1/4 and 3/4) is described as corner-shared tilted-squares, where a four-fold axis is located at the center of each square (Fig. 1(b)). The kinetics of sigma-phase precipitation in these high-temperature structural materials is generally very slow, in particular for austenitic steels and Ni-based superalloys so that in many cases, precipitates appear only after many thousand hours during high-temperature usage [1–7]. While precipitation of the sigma-phase compound is believed not to be significantly harmful to high-temperature mechanical properties (i.e., during high-temperature service), it can be detrimental to ambient-temperature mechanical properties (i.e., after cooling from high-temperature service), as the sigma-phase compound above some critical volume fraction (of a level below a several %) embrittles these structural materials, reducing the ductility and toughness as well as the impact strength. This is well known as 'sigma-phase embrittlement' that occurs in austenitic steels

* Corresponding author at: Department of Materials Science and Engineering, Kyoto University, Sakyo-ku, Kyoto 606-8501, Japan.
E-mail address: kishida.kyosuke.6w@kyoto-u.ac.jp (K. Kishida).

https://doi.org/10.1016/j.actamat.2023.118829
Received 11 September 2022; Received in revised form 13 February 2023; Accepted 2 March 2023
Available online 4 March 2023

and Ni-based superalloys and very significantly in ferritic steels [1,4,5,7]. For these phenomena, the sigma-phase compound has been regarded as one of the typical embrittling phase in many high-temperature structural materials based on iron and nickel [1–6]. Fundamental understanding of physical, chemical and structural properties of the sigma-phase compounds is thus indispensable for the mitigation of 'sigma-phase embrittlement'. However, while the sigma-phase compound itself has been supposed to be brittle since the discovery by Bain and Griffiths in 1927 [9], it is not clear at all how brittle the sigma-phase compound is and whether the brittleness and fracture of the precipitate itself and/or its interfacial decohesion from the adjacent matrix causes these phenomena. This uncertainty stems from the fact that there is no detailed study on plastic deformation of any of the sigma-phase compounds in the past. However, the plastic deformation behavior of β-uranium may give some insight into the deformability and brittleness of the sigma-phase compound, as β-uranium [10] is basically isostructural with FeCr [8][1]. Holden [11] identified the operation of {110}<001> slip in single crystals of β-uranium at room temperature among four different slip systems ({110}<001>, (001)<110>, {140}[001] and (001) <140>) that he predicted to operate. Subsequently, Kronberg [12] proposed the concept of zonal dislocation, in which cooperative and rotary-type atomic shuffling occurs in an atomic slab called 'shear zone' during dislocation motion, for the operation of {110}<001>. Rodriguez et al. [13] then identified the operation of {100}<001> slip in addition to {110}<001> slip and proposed extended dislocation that is different from the zonal dislocation proposed for {110}<001> slip and involves a high-energy planar fault formed between two Frank partial dislocations for {100}<001> slip. Although plastic flow is observed even at room temperature for β-uranium, our preliminary investigation clearly indicates that plastic flow cannot be observed for FeCr, the prototype of the sigma-phase compounds, in its single-phase bulk form even the temperature is increased to 700°C (Fig. S1).

Recently, however, micropillar compression testing [14,15] that uses a small specimen whose size is reduced to the micrometer scale has been recognized progressively as a powerful technique to study mechanisms

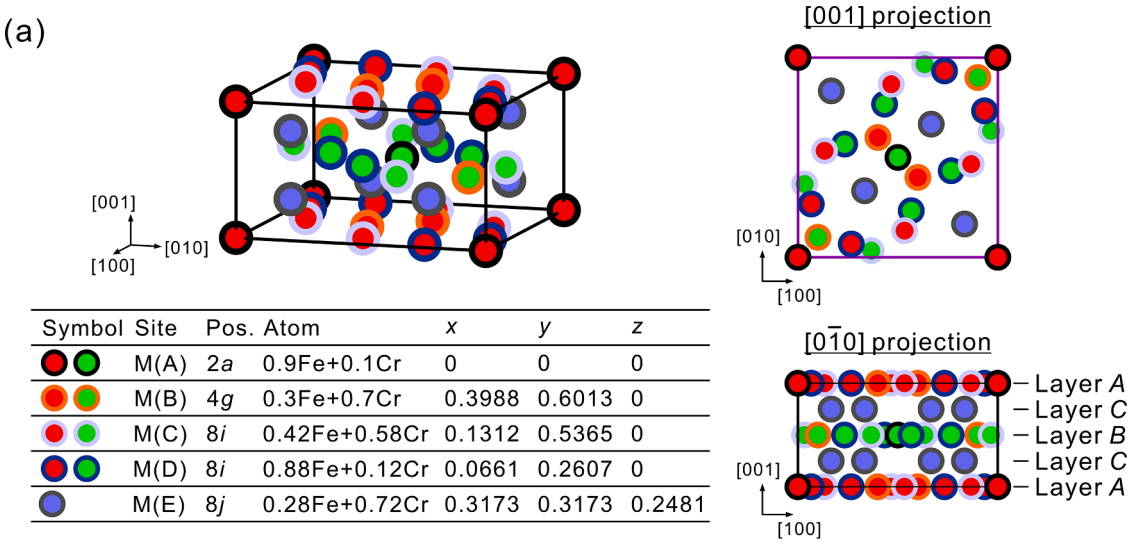

Symbol	Site	Pos.	Atom	x	y	z
	M(A)	2*a*	0.9Fe+0.1Cr	0	0	0
	M(B)	4*g*	0.3Fe+0.7Cr	0.3988	0.6013	0
	M(C)	8*i*	0.42Fe+0.58Cr	0.1312	0.5365	0
	M(D)	8*i*	0.88Fe+0.12Cr	0.0661	0.2607	0
	M(E)	8*j*	0.28Fe+0.72Cr	0.3173	0.3173	0.2481

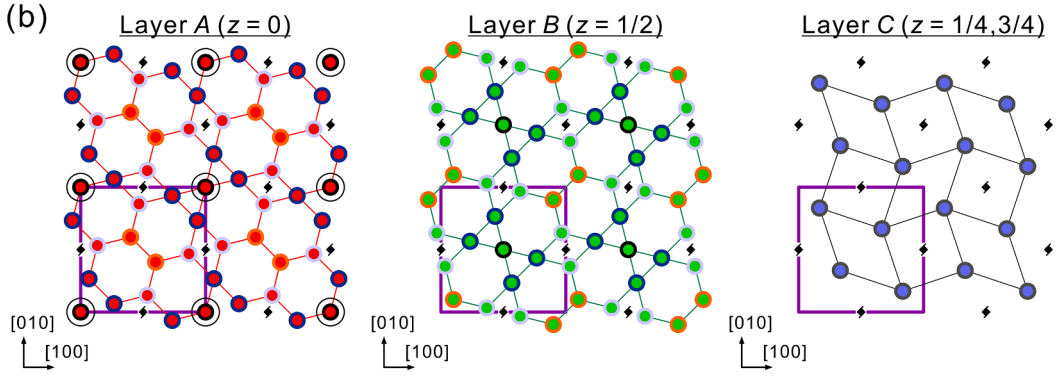

Fig. 1. (a) Crystal structure of sigma FeCr and (b) atomic arrangements of three types of atomic layers *A, B* and *C*. Open circles in layer *A* ($z = 0$) of (b) indicate the lattice points. Black squares with two additional arms in (b) indicate 4_2 screw axes parallel to the *c*-axis.

[1] The space group $P4_2/mnm$ and Pearson symbol $tP30$ are assigned to both the A_b structure of β-uranium and the $D8_b$ structure of the sigma-phase compounds. Atomic positions are identical for these two structures if distinction is not made for unlike atoms in the intermetallic compound FeCr. These two structures are indeed isostructural with each other, since all five crystallographic sites occupied in sigma FeCr are of the mixed occupancy of Fe and Cr atoms.

of plastic flow occurring at ambient temperature for brittle materials, and some examples can be seen in [16–29]. Slip systems operative at room temperature and their critical resolved shear stress (CRSS) values can be determined by this technique without being disturbed by severe oxide formation on the specimen surface as well as dislocation climb, which often occur during deformation of bulk specimens of brittle materials at high temperatures. Indeed, our preliminary investigation of the

sigma-phase compound FeCr by micropillar compression testing has identified the operation of {110}<001> slip at room temperature accompanied by a very high CRSS value of about 1.6 GPa for a particular crystal orientation of [$\bar{5}$ 6 11] [29]. On top of that, the zonal dislocation proposed by Kronberg [12] to operate for {110}<001> slip was indeed directly observed by atomic-resolution scanning transmission electron microscopy (STEM) for the first time [29]. Any other slip systems may operate with different CRSS values when specimens with other crystal orientations are tested. This has yet to be done.

In the present study, we investigate the plastic deformation behavior of single crystals of the sigma-phase compound FeCr in compression as a function of crystal orientation at room temperature with the use of micropillar specimens of a size range of 0.8~10.1 μm, in order to clarify the ambient-temperature deformation mechanism of the sigma-phase compound through identifying all the operative slip systems in the sigma-phase compound and evaluating their CRSS values.

2. Experimental Procedure

Ingots of a BCC solid solution phase with a nominal composition of Fe-50 at.%Cr were prepared by Ar arc-melting of high-purity Fe (>99.99%) and Cr (>99.9%). A specimen with approximate dimensions of 11×14×3.5 mm^3 cut from the ingot by spark machining was cold-rolled to 40 % in thickness reduction. Then, the cold-rolled specimen was encapsulated in a quartz ampoule with Ar gas and was heat-treated at 740°C for 116 hours, followed by air-cooling. The formation of the sigma-phase without any traces from other phases was confirmed by powder x-ray diffraction with a Rigaku MiniFlex II apparatus (Fig. S2). The lattice parameters estimated by powder X-ray diffraction were a = 0.8838 nm and c =0.4569 nm, both of which were a bit larger than those reported for FeCr with compositions near Fe-50 at.%Cr [8,30]. After mechanical polishing with diamond paste to mirror finish and analyzing crystallographic orientations of individual grains by electron back-scatter diffraction (EBSD) in a JEOL JSM-7001FA field-emission scanning electron microscope (FE-SEM), single-crystal micropillar specimens with square cross-sections having aspect ratios of ~3:1 (height to edge length) were machined from the annealed specimen (average grain size of about 300 – 700 μm) with a JEOL JIB-4000 focused-ion beam (FIB) apparatus at an operating voltage of 30 kV. The edge lengths (L) of the square cross-sections (referred to as "specimen size" in this paper) ranged from 0.8 to 10.1 μm. A square cross-section was employed to facilitate the identification of slip planes and slip directions. Three different compression-axis orientations (B: [$\bar{1}$ 11 28], C: [$\bar{8}$92] and D: [$\bar{13}$ 28 7]) were selected (Fig. 2(a)). For the A orientation ([$\bar{5}$ 6 11]) plotted in Fig. 2(a), the operation of {110}[001] slip was confirmed in our previous study [29]. The highest Schmid factors for some possible slip systems are listed in Table 1 for each orientation. The possible slip systems in Table 1 were selected on the assumption that those systems with shorter Burgers vectors (**b**) are preferred to operate. According to the magnitudes of Burgers vectors and Schmid factor values, the operation of {100}[001] slip is expected for the B orientation, while {100}<010> slip is expected for the C orientation. For the D orientation, {111}<0$\bar{1}$1> slip with a somewhat longer Burgers vector of the <101>-type may operate, as the Schmid factors for those with shorter Burgers vectors of the [001]- and <100>-types are relatively small. Based on these expectations, one of the two orthogonal side faces of each micropillar specimen was set parallel to the expected slip direction, so that the slip direction is easily determined from the appearance of slip traces on two orthogonal side faces after deformation, i.e., only faint traces should appear on the side face containing the slip direction, whereas distinct traces appear on the other.

Table 1
The highest Schmid factors for some possible slip systems for orientations A~D. The Schmid factor values for the identified slip systems are indicated in bold letters.

Slip system	b (nm)	A [$\bar{5}$ 6 11]	B [$\bar{1}$ 11 28]	C [$\bar{8}$92]	D [$\bar{13}$ 28 7]
{110}[001]	0.4569	**0.4739**	0.3705	0.0851	0.1086
{100}[001]		0.3656	**0.4803**	0.0637	0.1049
{100}<010>	0.8838	0.3214	0.0332	**0.4929**	0.3768
{001}<010>		0.3656	0.4803	0.0637	0.1049
{100}<0$\bar{1}$1>	0.9949	0.4534	0.2500	0.4671	0.3829
{011}<0$\bar{1}$1>		0.2274	0.3866	0.2601	0.3862
{111}<0$\bar{1}$1>		0.3784	0.3720	0.4082	**0.4813**

Compression tests were conducted for micropillar specimens with a flat punch indenter tip on an Agilent Technologies Nano Indenter G200 nanomechanical tester at room temperature under the displacement-rate-controlled mode at a nominal strain rate of 1×10^{-4} s^{-1}. Slip planes were determined by slip trace analysis made on two orthogonal surfaces of the deformed micropillar specimen by scanning electron microscopy (SEM) with a JEOL JSM-7001FA electron microscope. Deformation microstructures developed in the deformed micropillars were investigated by transmission electron microscopy (TEM) and scanning transmission electron microscopy (STEM) with JEOL JEM-2100F and JEM-ARM200F electron microscopes. Specimens for TEM/STEM observations were prepared by FIB-SEM in-situ lift-out technique using a FEI Quanta 3D 200i Dual-Beam system equipped with an Omniprobe nanomanipulator.

Single cantilever bend tests were conducted at room temperature for chevron-notched micro-beam specimens illustrated in Fig. 2(b) and (c), as described previously [21]. A notch plane was set parallel to (100) and (001), and a constant displacement rate of 5 nm s^{-1} was employed. The fracture toughness, K_{IC} was evaluated with the maximum load (P_{max}) reached during the test through numerical analysis using the following equations proposed by Deng et al. [31,32] with specimen dimensions of l = 12 μm, W = 4.5 μm and B = 3 μm, and notch lengths a_0 and a_1, and crack length a,

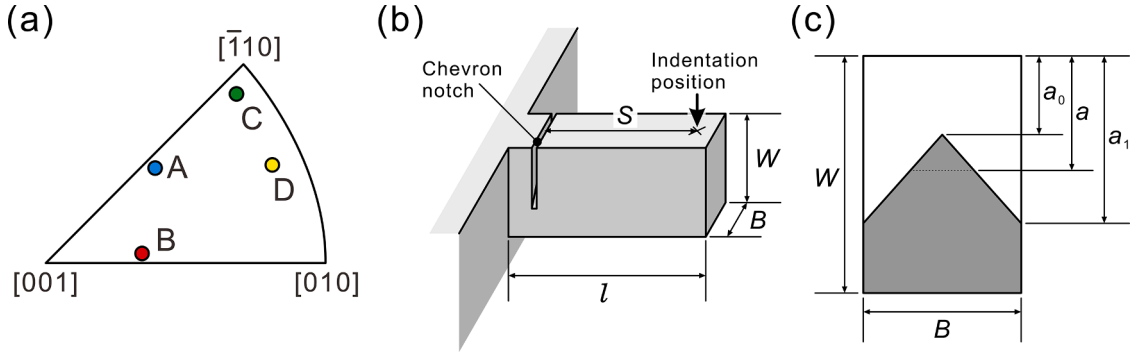

Fig. 2. (a) Standard stereographic projection of the loading-axis orientations and schematic illustration of (b) a chevron-notched micro-beam specimen for single cantilever bend test and (c) the shape of a chevron-notch.

$$K_{IC} = \frac{P_{\max}}{B\sqrt{W}} Y_C(\alpha_0, \alpha_1) \quad (1)$$

and

$$Y_C(\alpha_0, \alpha_1) = \sqrt{\frac{1}{2}\frac{dC_V(\alpha)}{d\alpha}\frac{\alpha_1 - \alpha_0}{\alpha - \alpha_0}}\Bigg|_{\alpha=\alpha_C} \quad (2)$$

where $P_{\max}$ is the maximum load, $Y_C(\alpha_0, \alpha_1)$ is the dimensionless geometry factor, $C_V(\alpha)$ is the compliance of the specimen, $\alpha_0 = a_0/W$, $\alpha_1 = a_1/W$, $\alpha = a/W$, $\alpha_C = a_C/W$, and a_C is a critical crack length [31,32].

3. Results

3.1. Elastic constants calculation

Elastic constants of sigma FeCr were calculated by the stress-strain method proposed by Le Page and Saxe [33] based on first-principles density functional theory (DFT) using the Vienna Ab initio Simulation Package (VASP) for 0 K [34]. The crystal structure of sigma FeCr is composed of five crystallographic sites, labelled as M(A) (Wyckoff position: 2*a*), M(B) (4*g*), M(C) (8*i*), M(D) (8*i*) and M(E) (8*j*), all of which are of the mixed occupancy of Fe and Cr atoms [8,30]. For the elastic constant calculation, a hypothetical ordered structure, in which M(A), M(B) and M(D) sites are fully-occupied by Fe, and the remaining sites of M(C) and M(E) are fully-occupied by Cr, was selected as a model structure. This is because the ordered structure has a chemical composition of Fe - 53.3at.% Cr, which is close to Fe-50 at.%Cr investigated in this study. The selection of the ordered structure is considered to be reasonable because the ordered structure has been reported to have the lowest formation energy among all possible ordered structures for chemical compositions near Fe-50 at.%Cr [35]. The generalized gradient approximation of Perdew-Burke-Ernzerhof (GGA-PBE) is used to treat the exchange-correlation functional [36]. An energy cutoff of 700 eV and a Monkhorst-Pack *k*-point mesh of 8 × 8 × 14 were used [37]. All calculations were performed for a non-spin polarized state considering the fact that sigma FeCr is non-magnetic at ambient temperatures [38,39]. The optimized lattice constants estimated with the standard unit cell with the hypothetical ordered structure were $a = 0.8649$ nm and $c = 0.4429$ nm, which are in good agreement with the experimental values obtained in this study and those previously reported [8,30]. Calculated values of single-crystalline elastic constants C_{ij} are listed in Table 2. The C_{ij} values for a spin polarized state are also listed in Table 2 for comparison. (Detailed comparisons of the calculation results for the non-spin polarized and spin polarized states are summarized in supplementary tables S1-S3.) Polycrystalline (isotropic) bulk modulus (*K*), shear modulus (*G*), Young's modulus (*E*) and Poisson's ratio (*ν*) values calculated from the single-crystalline elastic constants for 0 K with the Voigt-Reuss-Hill (VRH) approximation are 268.5 GPa, 124.2 GPa, 322.7 GPa and 0.2997, respectively, for the case of a random crystallographic texture.

3.2. Stress-strain behavior and slip trace observation

For the A orientation ([$\bar{5}$ 6 11]), the operation of {110}[001] slip was confirmed in our previous study [29]. Fig. 3(a)-(c) show selected stress-strain curves obtained for micropillar specimens with the B, C and D orientations, respectively. Compression tests were interrupted in most cases prior to failure for enabling detailed slip line observations. Stress-strain curves obtained for micropillar specimens with the A orientation can also be found in Fig. 3 of [29]. Strain bursts corresponding to flat portions of stress-strain curves are sometimes observed to occur soon after yielding with the magnitude of strain for each burst and the occurrence of strain burst itself both being dependent on individual specimen without any definite trend in terms of crystal orientation, specimen size and stress level. When strain bursts were detected, the yield stress was defined as the stress at which the first strain burst occurs. Otherwise, the yield stress was defined as the elastic limit. These yield stresses usually exceed 3 GPa and are indicated by arrows in the figures. For all orientations, plastic flow was clearly observed to occur regardless of specimen size investigated with the yield stress generally decreasing with the increase in specimen size for each orientation. The deformability of specimens with the C orientation is particularly high at room temperature, as failure does not occur even the strain level exceeds 5 %. It is thus evident that the sigma-phase compound FeCr is fairly deformable in compression at room temperature in the micropillar form, unlike in the bulk form (Fig. S1).

Fig. 4(a)-(c), (d)-(f) and (g)-(i) show SEM secondary electron images of deformation structures observed on two orthogonal surfaces of the micropillar with the B, C and D orientations, respectively. The observations were made along the direction inclined by 30° from the loading axis. For the B ([$\bar{1}$ 11 28]) orientation (Fig. 4(a)-(c)), straight slip lines are clearly observed on the (4 $\overline{44}$ 17) surface (Fig. 4(a)), while slip lines observed on the (11 1 0) surface are fairly faint (Fig. 4(c)). Slip trace analysis on the two orthogonal surfaces indicates the occurrence of slip on (010). The faint slip lines on the (11 1 0) surface indicates that the slip vector is contained in the (11 1 0) plane. Stereographic analysis has revealed that the slip direction is parallel to [001]. The slip system thus identified to operate in the micropillar with the B orientation is (010)[001]. This slip system is identical with that observed by Rodriguez et al. [13] for β-uranium in addition to {110}<001> slip.

For the C ([$\bar{8}$92]) orientation (Fig. 4(d)-(f)), straight slip traces are clearly observed on the (18 16 1) surface (Fig. 4(f)), while rather faint slip traces are observed along two different directions on the (0$\bar{2}$9) surface (Fig. 4(d)). Slip trace analysis confirms that slip deformation occurs on (100) and (010) planes. The faint slip lines for the trace of (010) on the (0$\bar{2}$9) surface indicate the slip direction along [100], confirming the operation of (010)[100] slip. Another set of slip lines observed on the (0$\bar{2}$9) surface corresponds to (100)[010] slip that is equally stressed with (010)[100] slip in the C orientation. The slip system thus identified to operate for the C orientation is {100}<010>, which has never been identified and even considered previously in β-uranium [11–13].

For the D ([$\overline{13}$ 28 7]) orientation (Fig. 4(g)-(i)), straight slip traces are observed on the ($\bar{3}$ $\bar{4}$ 11) surface (Fig. 4(i)), while slip traces observed on the (35 13 13) surface are only faint (Fig. 4(g)). Slip trace analysis on the two orthogonal surfaces indicates the occurrence of slip on ($\bar{1}$11). The faint slip lines on the (35 13 13) surface indicate that the slip direction is contained in the (35 13 13) plane. Stereographic analysis has revealed that the slip direction is parallel to [0$\bar{1}$1]. The slip system thus identified to operate in the micropillar with the B orientation is ($\bar{1}$11)[0$\bar{1}$1]. This slip system has never been identified and even considered previously in β-uranium [11–13].

In addition to {110}[001] that we identified in our previous study [29], three different slip systems ({100}[001], {100}<010> and {111}<0$\bar{1}$1> are identified in the present study to operate at room temperature in the sigma-phase compound FeCr. The latter two systems are those identified in the present study for the first time to be operative in the crystals with the $D8_b/A_b$ structure.

Table 2
The calculated elastic constants C_{ij} (in GPa) for FeCr with a chemical composition of Fe - 53.3at.% Cr. Crystallographic sites of M(A), M(B) and M(D) are assumed to be fully-occupied by Fe, while those of M(C) and M(E) are fully-occupied by Cr.

	C_{11}	C_{33}	C_{44}	C_{66}	C_{12}	C_{13}
Non-spin polarized	452.3	495.6	110.0	111.8	194.2	157.0
Spin polarized	394.2	454.8	106.7	110.7	143.0	127.5

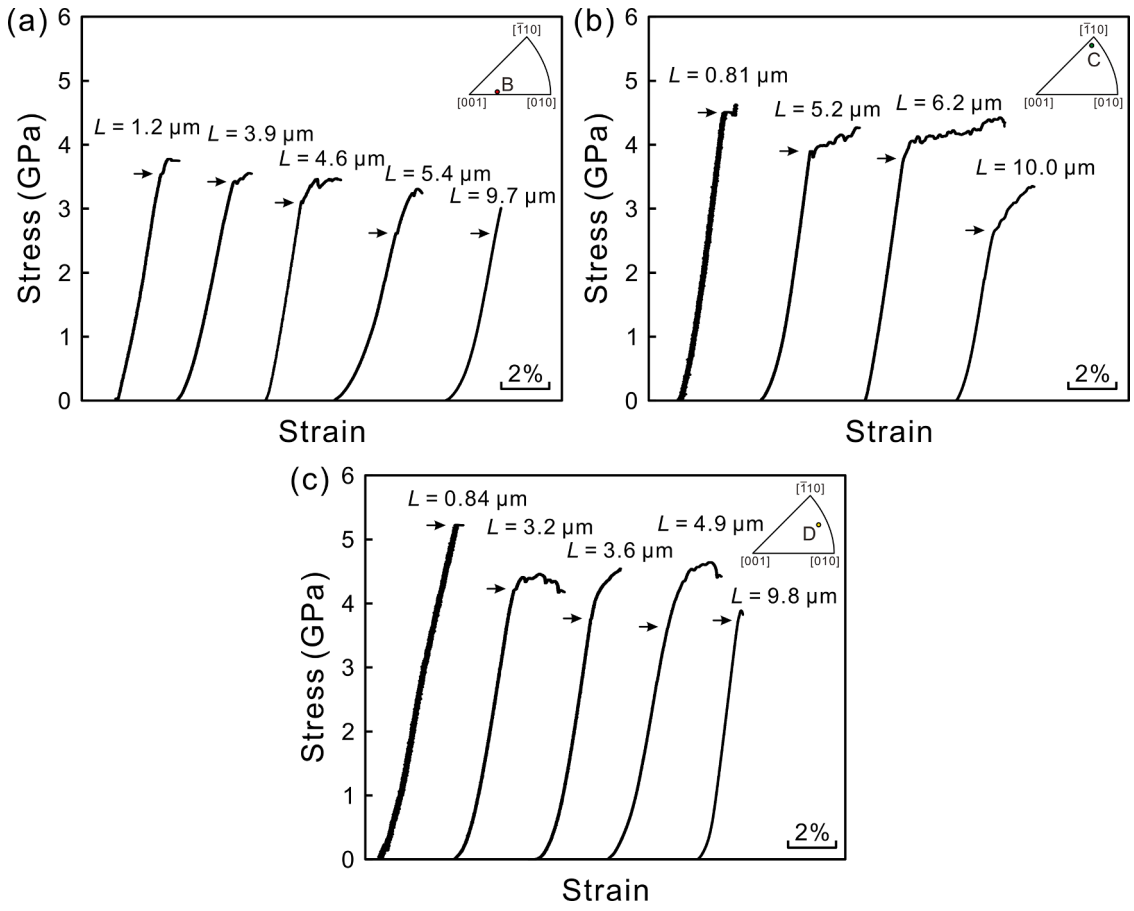

Fig. 3. Selected stress-strain curves obtained for micropillar specimens with (a) B ([$\bar{1}$ 11 28]), (b) C ([$\bar{8}$92]) and (c) D ([$\bar{13}$ 28 7]) orientations, respectively. Arrows indicate the yield points deduced either as the elastic limit or as the stress at which the first strain bust occurs.

3.3. Dislocation structure and dissociation

In our previous paper [29], we identified the [001] dislocation of the {110}[001] slip system (for the orientation A) is of the zonal type, in which complex atomic shuffling occurs within each of (001) Kagome atomic layers in a shear zone bounded by the slip planes of the composite dislocations [12,29]. Of interest to examine is whether the [001] dislocation gliding on {100} is also of the zonal-type or not. Fig. 5(a)-(c) show bright-field images of dislocations with the Burgers vector (**b**) of [001] observed in a thin foil cut nearly parallel to the (010) slip plane in a micropillar specimen with the B orientation taken with different diffraction vectors (**g**). Dislocations visible with **g**=00$\bar{2}$ (Fig 5(a)) are invisible with **g**=200 (Fig 5(b)) and **g**=4$\bar{1}$0 (Fig 5(c)), confirming their Burgers vector of [001]. Many of dislocations imaged are all in near edge character. A weak-beam dark-field image of Fig. 5(d) indicates that these dislocations with **b** = [001] are not dissociated into partial dislocations on the (100) slip planes.

Atomic-resolution (high-angle annular dark-field) HAADF-STEM imaging of a [001] dislocation introduced in a micropillar specimen with the B orientation was made to gain further information of the core structure of the [001] dislocation gliding on (010), as shown in Fig. 6. The thin foil was cut parallel to (100) so as to observe the [001] edge dislocation end-on. Burgers circuit construction around the dislocation confirms that the Burgers vector of the dislocation is **b** = [001]. By locating the extra-half planes parallel to (001), two partial dislocations with an identical Burgers vector of **b** = 1/2[001] are observed at positions marked by symbols ⊥ on two (010) planes separated by a distance corresponding approximately to 1.5*a* (*a*: the a-axis lattice parameter). The atomic arrangements on both, the left- and right-hand sides of these partial dislocations are identical to those of the perfect crystal, confirming that no stacking fault is formed on either side of each of the partial dislocations. These characteristics clearly deny the existence of the extended dislocation involving a planar fault of the high-energy type as proposed by Rodriguez et al. [13] but suggest that the observed [001] dislocation is also of the zonal-type, which we identified for {110}[001] slip in our previous study [29]. The [001] zonal dislocation identified in the present study also involves atomic shuffling in the shear zone bordered by the (010) glide planes for these two partial dislocations upon their motion. The details of atomic shuffling in the shear zone will be discussed in detail in section 4.2.

Fig. 7(a) shows a weak-beam dark-field image of dislocations with **b** = [010] observed in a thin foil cut nearly parallel to the (100) slip plane in a micropillar specimen with the C orientation. All [010] dislocations are clearly dissociated into two partial dislocations (Fig. 7(a) and (b)). For this orientation, the (100)[010] slip system is identified by trace analysis of deformation markings on the micropillar specimen surfaces (Fig. 4(d)-(f)). The [010] dislocation responsible for (100)[010] slip cannot be of the zonal-type, as the [010] slip direction is contained in the (001) plane, on which complex atomic shuffling is thought to occur within each of (001) Kagome atomic layers [12,29]. All [010] dislocations imaged in Fig. 7(a) are clearly observed to dissociate into two collinear partial dislocations, as both partial dislocations seen in Fig. 7 (b) (the frame area in Fig. 7(a)) imaged with **g**=022 are simultaneously invisible when imaged with **g**=004 (Fig. 7(c)) and with **g**=202 (Fig. 7 (d)). The dissociation width of the dislocation in Fig. 7(b) (with the line vector approximately 78° from the Burgers vector) is very wide, about 34 nm on the (100) slip plane. Possible dislocation dissociation schemes for [010] dislocations on {100} slip planes will be discussed in the section 4.3.

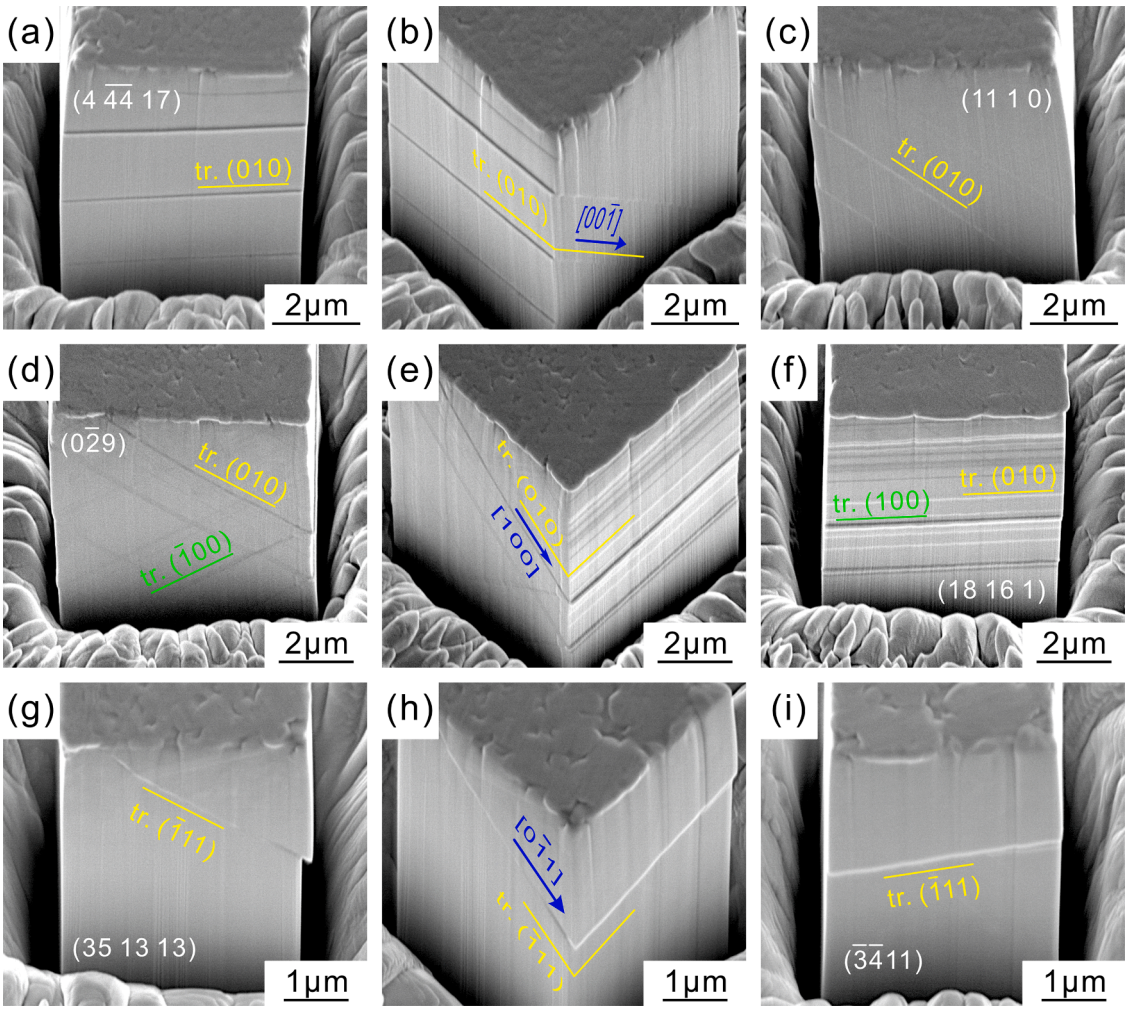

Fig. 4. Deformation markings observed on two orthogonal surfaces of FeCr single crystalline micropillars with (a)-(c) B (L = 5.4 μm), (d)-(f) C (L = 6.2 μm) and (g)-(i) D (L = 3.6 μm) orientations.

Fig. 8(a) shows a bright-field image of dislocations with **b** = [0$\bar{1}$1] observed in a thin foil cut nearly parallel to the ($\bar{1}$11) slip plane in a micropillar specimen with the D orientation. For this orientation, the ($\bar{1}$11)[0$\bar{1}$1] slip system is identified by trace analysis of deformation markings on the micropillar specimen surfaces (Fig. 4(g)-(i)). [0$\bar{1}$1] dislocations are observed to dissociate into three partials as clearly seen in a weak-beam image of Fig. 8(b). Because all partial dislocations are invisible simultaneously when imaged with **g** = [411] (Fig. 8(c)), [0$\bar{1}$1] dislocations are likely to dissociate into three partials with collinear Burgers vectors parallel to [0$\bar{1}$1]. Possible dislocation dissociation schemes for <0$\bar{1}$1> dislocations on {111} slip planes will also be discussed in section 4.3.

3.4. Fracture toughness

Load-displacement curves obtained in three-point bend tests for chevron-notched micro-beam specimens with a notch plane parallel to (100) and (001) are shown in Fig. 9(a). The fracture surfaces observed for the corresponding specimens are shown in Fig. 9(b) and (c). The fracture surfaces for both cases are fairly flat, suggesting the occurrence of cleavage fracture. The values of fracture toughness evaluated with Eqs. (1) and (2) are 1.8 ± 0.22 and 1.6 ± 0.16 MPa·m$^{1/2}$ respectively for a notch plane parallel to (100) and (001). These values of fracture toughness of FeCr are very low as comparable to those for some typical ceramics such as SiC (1.4~1.6 MPa·m$^{1/2}$) [23], indicative of significant brittleness of the sigma phase compound.

4. Discussion

4.1. Operative slip systems

The slip systems identified in our previous [29] and present studies to operate in the sigma-phase compound FeCr at room temperature in the micropillar form are {110}[001], {100}[001], {100}<010> and {111}<01$\bar{1}$>. Since there is no previous study to identify the slip systems in any sigma-phase compound, the present study is the first to identify the operative slip systems in sigma-phase compounds. Here, we compare these slip systems identified to operate in FeCr with those predicted and identified to operate in isostructural β-uranium [11–13]. Holden [11] predicted four slip systems ({110}[001], (001)<110>, {140}[001] and (001) <140>) to operate in β-uranium. Of the four systems, he himself [11] and later Rodriguez et al. [13] identified only {110}[001] slip to operate. We also did not observe the other three systems to be active in FeCr. Rodriguez et al. [13] identified the operation of {100}[001] slip in β-uranium. We also indeed observed this slip system to operate in FeCr. While the [001] zonal dislocation responsible for {110}[001] slip predicted by Kronberg [12] for β-uranium was proven to exist in FeCr [29], the [001] extended dislocation involving a planar fault of the high-energy type proposed for {100}[001] slip in β-uranium by Rodriguez et al. [13] was not observed in FeCr. Instead, the zonal dislocation similar to that responsible for {110}[001] slip was

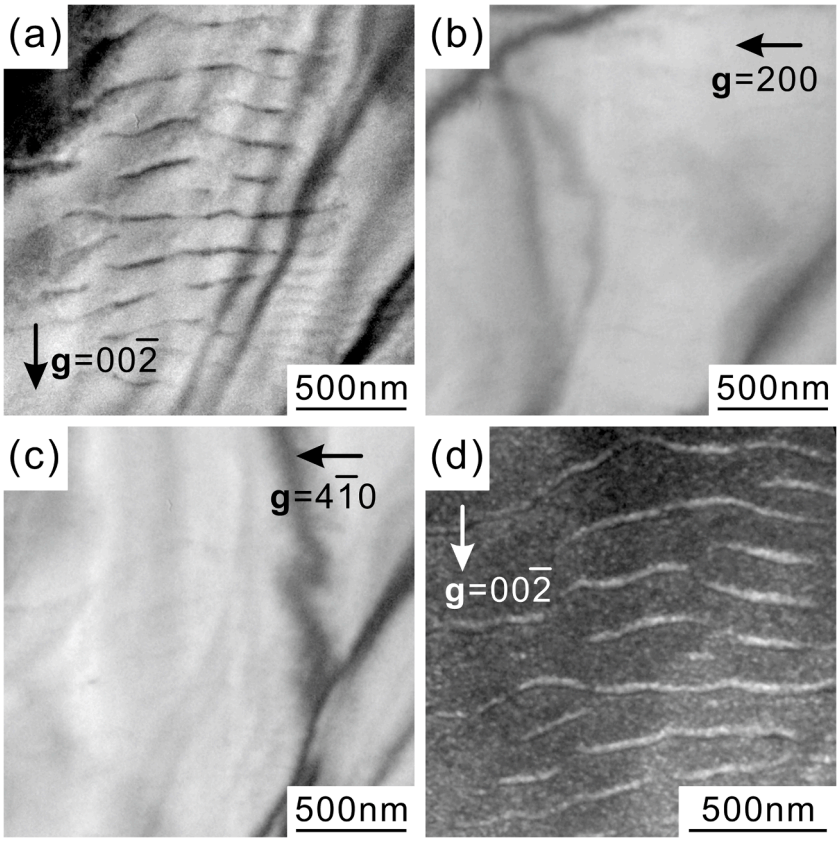

Fig. 5. Bright-field images of [001] dislocations on (010) introduced in a micropillar specimen with the B orientation taken with (a) **g**=00$\bar{2}$, (b) **g**=200 and (c) **g**=4$\bar{1}$0. Weak-beam image of the same area taken with **g**=00$\bar{2}$is shown in (d).

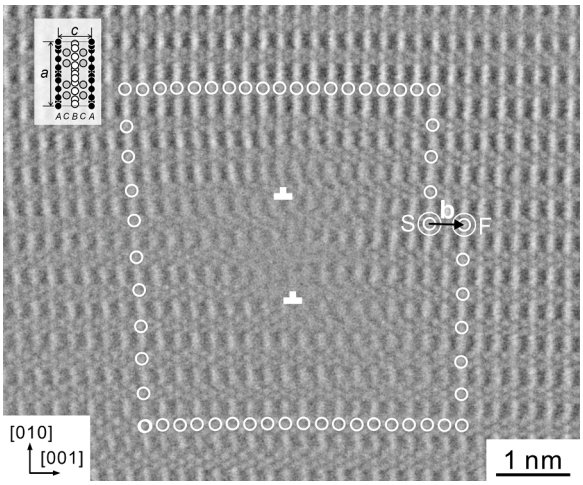

Fig. 6. Atomic-resolution HAADF-STEM image of a core structure of a [001] edge dislocation on (010) slip plane introduced in a micropillar specimen with the B orientation. Burgers circuit construction around the dislocation confirms that the Burgers vector of the dislocation is **b** = [001]. Two partial dislocations with an identical Burgers vector of **b** = 1/2[001] are at positions marked by symbols ⊥ on two (010) planes separated by a distance corresponding to 1.5*a*.

experimentally proven to exist in the present study. The details of atomic shuffling in the shear zone associated with the [001] zonal dislocation responsible for {100}[001] slip will be discussed in the next section.

4.2. [001] zonal dislocation responsible for {100}[001] slip

Within the crystal structure of the tetragonal $D8_b$-type, Atomic layers *A* (at $z = 0$) and *B* (at $z = 1/2$) both having the identical Kagome-type atomic arrangement are related to each other with the 90°-rotation relationship about the *c*-axis (Fig. 1). As in the atomic shuffling model that we proposed for the [001] zonal dislocation responsible for {110}[001] slip [29], atoms in atomic layers *A* and *B* are considered to shuffle cooperatively so that the atomic arrangement of atomic layer *A* gradually turns into that of Atomic layer *B* and vice versa within the shear zone (i.e., the core region) of the [001] dislocation gliding on (100). Fig. 10 shows a plausible atomic shuffling model for the [001] zonal edge dislocation on (100), which is constructed assuming that the boundaries defining the shear zone are located at positions indicated with dashed lines in Fig. 10. Similarly to our atomic shuffling model for the [001] zonal edge dislocation on {110}, all atomic shuffles are successfully selected so as to occur within each of (001) Kagome atomic layers without incorporating any translayer-type atomic shuffles that were involved in the original model for the (001) zonal dislocation on {110} by Kronberg [12].

The proposed model is constructed based on the assumption that all atoms in each of Kagome atomic layers shuffle so as to maintain the in-plane translation symmetry of the Kagome atomic layer at any step of shuffling. The assumption makes the model of atom shuffling the simplest with the smallest number of different atomic shuffle motions. With this assumption, the height of the shear zone is expected to simply be *na*, integer (*n*) multiples of the *a*-axis lattice parameter. Of significance to notice, however, is that if atomic layers *A* and *B* are not distinguished, the atomic arrangement similar to that observed at the shear zone boundary #Z1 appears periodically at an interval of *a*/2 (as indicated by arrows in Fig. 10(c)). This indicates that the height of the shear zone can be *na*/2, integer multiples of half the *a*-axis lattice

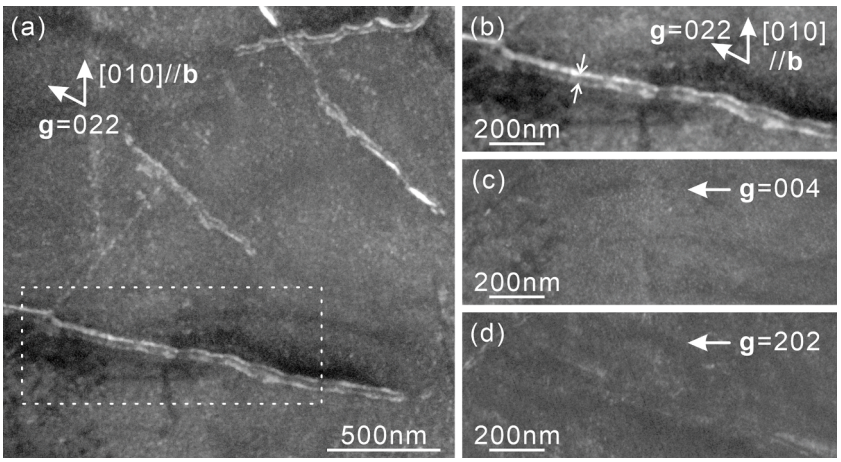

Fig. 7. (a) Weak-beam dark-field image of dislocations with **b** = [010] observed in a thin foil cut nearly parallel to the (100) slip plane in a micropillar specimen with the C orientation taken with **g** = 022. (b-c) Contrast analysis of dislocations in the marked area in (a) taken with (b) **g** = 022, (c) **g** = 004 and (d) **g** =202.

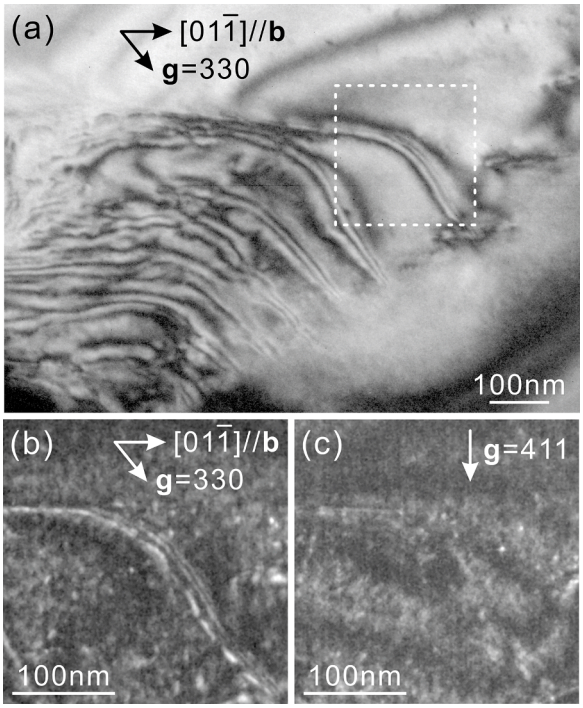

Fig. 8. (a) Bright-field and (b,c) weak-beam dark-field images of dislocations with **b** = [01$\bar{1}$] observed in a thin foil cut nearly parallel to the ($\bar{1}$11) slip plane in a micropillar specimen with the D orientation taken with (a,b) **g** = 330 and (c) **g** = 411.

parameter. If the shear zone height is selected so as to minimize the number of atoms to shuffle, the height must be the smallest one, i.e., $a/2$. But, the shear zone height actually observed by experiment is $3a/2$ ($1.5a$) (Fig. 6). We believe that elastic interaction between two composite partial dislocations with an identical Burgers vector of **b** = 1/2 [001] aligned nearly perpendicular to the {100} slip plane plays an important role in determining the shear zone height. Fig. 11 plots the force acting between two vertically-aligned parallel edge dislocations both with **b** = 1/2[001] as a function of the height of the shear zone. The force at the height of $1.5a$ is calculated to be only one third of that at $0.5a$, as the force is inversely proportional to the separation distance. Interestingly, the force at the height of $1.5a$ for the [001] zonal dislocation responsible for {100}[001] slip is comparable to that for the [001] zonal dislocation responsible for {110}[001] at the actually observed height of $\sqrt{2}a$ [29]. This further supports the importance of elastic interaction between two composite partial dislocations in determining the shear zone height.

4.3. Dislocation dissociation

We now discuss how the identified slip systems are selected on the basis of the atomic arrangement in the crystal structure of FeCr, in particular for {100}<010> and {111}<0$\bar{1}$1> slip, in which the relevant dislocations are identified not to be of the zonal type. This is particularly important when dislocations dissociate into partial dislocations. We now examine the energetic barrier along some possible slip directions on the observed slip planes by calculating the generalized stacking-fault energy (GSFE) or the overlapped atomic volumes involved in the dislocation glide process [40,41]. Because all crystallographic sites in the sigma-phase compounds are of the mixed occupancy of the constituent atoms, generalized stacking-fault energy (GSFE) calculations by first-principles density functional theory (DFT) as well as the overlapped atomic volume (OLAV) calculations were difficult to make. In the GSFE calculations, the hypothetical ordered structure used for calculating the elastic constants in section 3.1 was employed (see the detailed calculation method in Supplementary) to calculate those on the {100} plane with the smallest in-plane unit-cell. In the OLAV calculations, all sites in the crystal structure are assumed to be occupied exclusively by Fe atoms. This may not cause a significant problem since the Goldschmidt metallic radii for Fe (0.126 nm) and Cr (0.128 nm) atoms are very close to each other.

The GSFE on the {100} plane and the OLAVs on the {100} and {111} planes are depicted respectively in Fig. 12(a)-(c) as a function of displacement parallel to the respective Burgers vector (<010> and <0$\bar{1}$1> for the {100} and {111} planes). Since the observed dissociation schemes for <010> and <0$\bar{1}$1> dislocations are both of the collinear-type, we only consider the displacement parallel to their Burgers vectors. We considered seven and three crystallographically non-equivalent planes for the {100} and {111} planes (Fig. 12(d),(e)). For {100}<010> slip, characteristic features of GSFE (Fig. 12(a)) and OLAVs (Fig. 12(b)) are very similar to each other, indicating that the results of OLAV calculations can be used to predict plastic behaviors of the sigma-phase compounds such as possible slip systems, actual slip planes and dislocation dissociation as a first approximation. For (100)[010] slip, the GSFE and OLAV calculation both commonly indicate that the [010] dislocation dissociates into three colinear partial dislocations on many different {100} slip planes, as approximately described by

$$[010] \rightarrow 7/24[010] + 5/12[010] + 7/24[010] \quad (3)$$

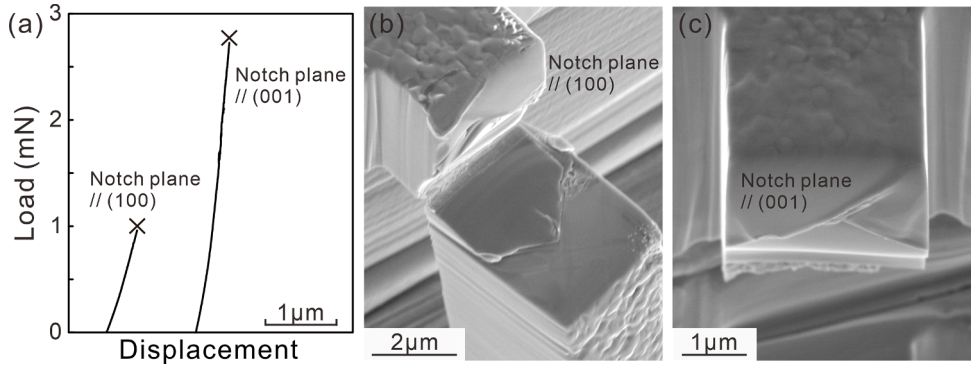

Fig. 9. (a) Load-displacement curves obtained in three-point bend tests for chevron-notched micro-beam specimens with a notch plane parallel to (100) and (001) and (b), (c) SEM secondary electron images of fracture surface of the corresponding specimens.

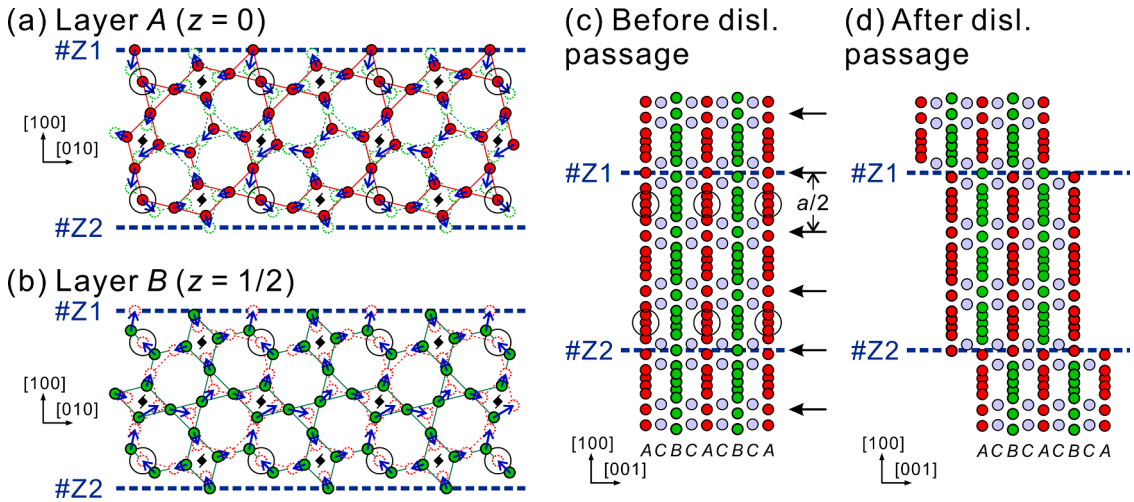

Fig. 10. Atomic shuffling model in atomic layers (a) *A* and (b) *B* of a (100)[001] zonal dislocation. Blue arrows indicate the shuffling directions and magnitudes for atoms so that atomic arrangement of Atomic layer *A* gradually turns into that of Atomic layer *B* and vice versa within the shear zone. Dashed lines #Z1-#Z2 indicate the pairs of glide planes defining the shear zones. (c,d) [010] projected views of sigma FeCr (c) before and (d) after one dislocation passage.

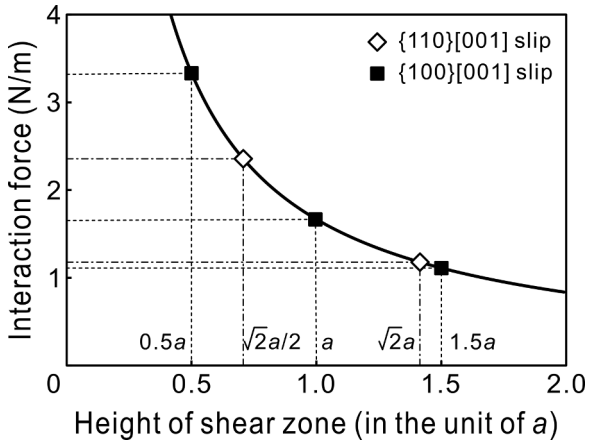

Fig. 11. Interaction force between two vertically-aligned parallel edge dislocations with an identical Burgers vector of $\mathbf{b} = 1/2[001]$ plotted as a function of the height of the shear zone.

This is somewhat different from what is observed by TEM (Fig. 7). Weak-beam TEM imaging revealed two-fold (instead of three-fold) dissociation with a relatively wide separation distance of about 34 nm for the 78°-mixed dislocation. The energy of stacking fault formed by the first leading partial dislocation with $\mathbf{b} = 7/24[010]$ is estimated to be about 187 mJ/m^2 using the isotropic elastic constants of $G = 124.2$ GPa and $\nu = 0.2997$ for 0 K. This stacking fault energy is by far smaller than that ($\sim$ 2500 mJ/m^2 on $\{100\}_e$ for 0 K) deduced by the DFT calculation. The reasons for these discrepancies regarding dislocation dissociation and stacking fault energy have yet to be clarified. From a theoretical perspective, temperature, spin polarization, ordered structure formation, and in-plane atomic relaxations are possible factors that should be further considered in calculating theoretical SFE values. From the experimental side, a closer investigation of the core structure of the [010] dislocation, gliding on (100) planes, is currently ongoing in our research group, to see if atomic shuffle motion is involved in addition to standard shear.

For (111)[0$\bar{1}$1] slip, two local minima in the overlapped atomic volume are found for displacement along [0$\bar{1}$1] when the [0$\bar{1}$1] dislocation glides on the $(111)_b$ slip plane (Fig. 12(c)). This indicates that the [0$\bar{1}$1] dislocation can dissociate into three colinear partial dislocations, as approximately described by

$$[0\bar{1}1] \rightarrow 19/50[0\bar{1}1] + 27/100[0\bar{1}1] + 7/20[0\bar{1}1]. \quad (4)$$

This is consistent with the results of the TEM observations (Fig. 8). The energies of the stacking faults formed by the first leading partial dislocation with $\mathbf{b} = 19/50[0\bar{1}1]$ and the second partial dislocation with $\mathbf{b} = 27/100[0\bar{1}1]$ are estimated, respectively, to be about 690 and 460 mJ/m^2, based on the separation distances of about 5.6 nm (between the first and second partials) and 10.2 nm (between the second and third

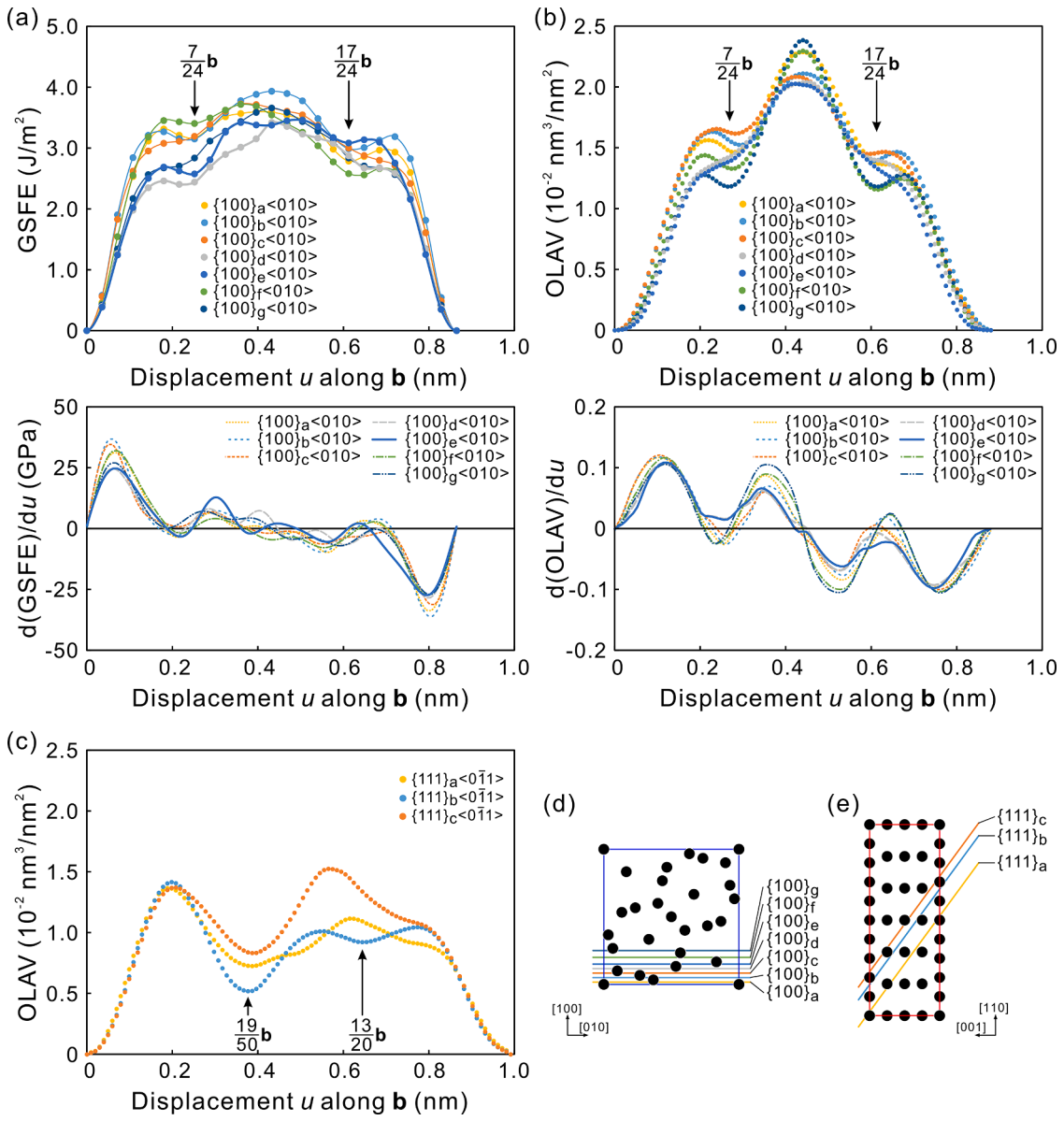

Fig. 12. (a) Generalized stacking fault energy (GSFE) and (b) overlap atomic volume (OLAV) curves together with their derivatives calculated for {100}<010> slip. (c) OLAV curves calculated for {111}<0$\bar{1}$1> slip. (d,e) Possible slip planes that are crystallographically non-equivalent for slip systems of (d) {100}<010> and (e) {111}<0$\bar{1}$1>. The plane indices with subscripts indicated in each of the figures correspond to the atomic planes on which the GSFE calculations and/or OLAV calculations were made.

partials) for the 60°-mixed dislocation (Fig. 8(b)).

4.4. Critical resolved shear stress

CRSS values for the four identified slip systems calculated with the yield stress values and the corresponding Schmid factors (Table 1) are plotted in Fig. 13 as a function of specimen size. While the CRSS values are essentially independent of specimen size for {110}[001] slip, an inverse power-law scaling is valid for {100}[001], {100}<010> and {111}<0$\bar{1}$1> slip in sigma FeCr with an exponent of 0.05, 0.1 and 0.1, all of which are much smaller than those usually reported for single crystals of FCC (face-centered cubic) (0.5~1.0) and BCC (body-centered cubic) (0.3~0.5) metals [20,42,43]. This may be closely related to the very high values of the Peierls stress (frictional stress) for these slip systems in FeCr.

Although the relation between the inverse power-law scaling for the specimen-size dependent CRSS and bulk CRSS value has often been discussed along different argumentation chains [22,44,45], the CRSS value obtained for micropillar specimens of FCC and BCC metals is known to usually approach the corresponding bulk value as the specimen size increases and the CRSS value can be regarded as the bulk one when the specimen size reaches 20~30μm [43]. On this basis, we can estimate the bulk CRSS values at room temperature to be 1.58, 1.45, 1.33 and 1.55 GPa for {110}[001], {100}[001], {100}<010> and {111}<0$\bar{1}$1> slip in FeCr. Since these four slip systems have the CRSS values not so different from each other (in the range of 1.33~1.58 GPa), there may be sufficient numbers of independent slip systems to ensure the general deformation of polycrystalline FeCr. The occurrence of premature failure in the sigma phase compound in the bulk form may then be ascribed to the very high CRSS values for these four slip systems combined with the very low fracture toughness (1.6~1.8 MPa·m$^{1/2}$). According to Ashby and coworkers [46–48], premature fracture of brittle materials occurs by cracks nucleated and propagated in a direction parallel to the compression axis originating from pre-existing flaws.

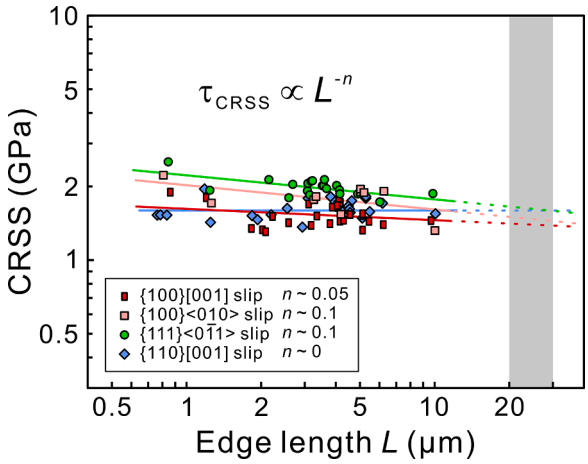

Fig. 13. Specimen size dependence of CRSS values for {110}[001], {100}[001], {100}<010> and {111}<0$\bar{1}$1> slip. The shaded area corresponds to the specimen size L range of 20−30μm, where the CRSS values coincide with those of the bulk specimens for most metallic materials.

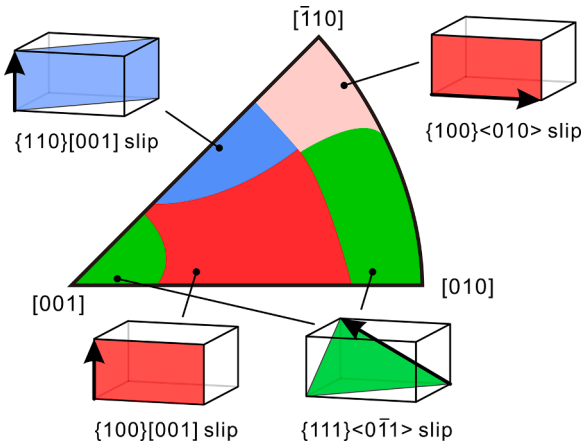

Fig. 14. Stereographic projection of slip systems expected to operate under uniaxial loading calculated based on the extrapolated bulk CRSS values for the four slip systems identified in this study.

The critical axial stress σ_C for crack initiation was estimated to be $CK_{Ic}/(\pi a)^{1/2}$, where a represents the size of a pre-existing flaw and C is a constant of the order of 1 depending on material, geometrical configuration of the pre-existing flaw and the number density of the flaws [46–48]. We can deduce a critical size of a pre-existing flaw to achieve very high axial stress in micropillar compression (≥ 2.5~5 GPa) to be of the order of several tens to hundreds of nanometers in FeCr with the low fracture toughness values. Consideration of such small flaws can be avoided in many cases in micropillar specimens of the micron-meter size, whereas they are inevitably occurring within bulk-sized specimens. This may be one of the reasons why plastic flow is not observed in specimens of bulk size.

Fig. 14 illustrates the orientation dependence of expected operative slip systems under uniaxial loading calculated based on the estimated bulk CRSS values for these four slip systems. In spite of the fact that {110}[001] slip has been observed to operate at room temperature as the primary slip system in β-uranium [11,13], the orientation range where {110}[001] slip operates is predicted not to be so wide in FeCr because of the high estimated bulk CRSS value. Instead, {100}[001] slip is expected to operate in a rather wide orientation range. These two slip systems are expected to operate in a wide orientation range in the middle of the standard triangle in the stereographic projection. Plastic flow was proven to be carried by zonal dislocations for both {110}[001] and {100}[001] slip. Since complex atomic shuffling in the shear zone is needed for the motion of these zonal dislocations, their mobility is expected not so high in particular at ambient temperature. This may also be one of the reasons why plastic flow is not observed in specimens of the bulk size.

5. Conclusions

The results of micropillar compression tests on single crystals of the sigma-phase compound FeCr made at room temperature as a function of the loading axis orientation and specimen size are summarized as follows.

1. Three slip systems, {100}[001], {100}<010> and {111}<0$\bar{1}$1> are identified to be operative in sigma FeCr at room temperature, in addition to {110}[001] we previously identified. The CRSS values for {100}[001], {100}<010> and {111}<0$\bar{1}$1> slip are very high, all exceeding 1.3 GPa. The CRSS value increases with the decrease in the specimen size following the inverse power-law relationship with an exponent of 0.05, 0.1 and 0.1, respectively. The bulk CRSS values are deduced to be 1.45, 1.33 and 1.55 GPa respectively for these three slip systems.
2. Atomic-resolution STEM imaging of the core structure of a [001] dislocation in edge character confirms that the [001] dislocation gliding on the (100) plane is of the zonal-type, as in the case of the [001] dislocation gliding on the (110) plane. A plausible atomic shuffling model for the {100}[001] zonal dislocation is proposed.
3. Both <010> dislocations responsible for {100}<010> slip and <0$\bar{1}$1> dislocations responsible for {111}<0$\bar{1}$1> slip are confirmed not to be of the zonal-type and to dissociate into two and three partial dislocations with collinear Burgers vectors, respectively.
4. Elastic constants for a hypothetical ordered structure with a chemical composition of Fe - 53.3at.% Cr are calculated to be $C_{11} = 452.3$ GPa, $C_{33} = 495.6$ GPa, $C_{44} = 110.0$ GPa, $C_{66} = 111.8$ GPa, $C_{12} = 194.2$ GPa, $C_{13} = 157.0$ GPa by the first-principles DFT calculation assuming a non-polarized state.
5. The fracture toughness values are evaluated to be 1.8 ± 0.22 and 1.6 ± 0.16 MPa·m$^{1/2}$ respectively for a notch plane parallel to (100) and (001) by micro-cantilever bend tests for chevron-notched microbeam specimens. These low fracture toughness values indicate significant brittleness of sigma FeCr.

Declaration of Competing Interest

The authors declare that they have no known competing financial interests or personal relationships that could have appeared to influence the work reported in this paper.

Acknowledgements

This work was supported by Grant-in-Aids for Scientific Research on innovative Areas on High Entropy Alloys through the grant number JP18H05450 and JP18H05451, and in part by JSPS KAKENHI grant numbers JP18H05478, JP19H00824, JP19K22053, JP20K21084 and JP21H01651 and by the Elements Strategy Initiative for Structural Materials (ESISM) from the Ministry of Education, Culture, Sports, Science and Technology (MEXT) of Japan (Grant number JPMXP0112101000), and in part by JST CREST (Grant number JPMJCR1994). HI acknowledges the support from the Alexander von Humboldt Foundation for their cooperative research conducted under the Humboldt Fellowship of HI.

Supplementary materials

Supplementary material associated with this article can be found, in

the online version, at doi:10.1016/j.actamat.2023.118829.

References

[1] E.O. Hall, S.H. Algie, The sigma phase, Metall. Rev. 11 (1966) 61–88.
[2] M.H. Lewis, Precipitation of (Fe, Cr) sigma phase from austenite, Acta Metall. 14 (1966) 1421–1428.
[3] R.F. Decker, C.T. Sims, The metallurgy of nickel-base alloys, in: C.T. Sims, W. C. Hagel (Eds.), The Superalloys, Eds, John Wiley & Sons, New York, 1972, pp. 33–77.
[4] D.M.E. Villanueva, F.C.P. Junior, R.L. Plaut, A.F. Padilha, Comparative study on sigma phase precipitation of three types of stainless steels: austenitic, superferritic and duplex, Mater. Sci. Tech. 22 (2006) 1098–1104.
[5] C.-C. Hsieh, W. Wu, Overview of intermetallic sigma (σ) phase precipitation in stainless steel, ISRM Metall. (2012) (2012), 732471.
[6] H.M. Tawancy, On the precipitation of intermetallic compounds in selected solid-solution-strengthened Ni-base alloys and their effects on mechanical properties, Metallogr. Microstruct. Anal. 6 (2017) 200–215.
[7] A.L. Shaeffler, Constitution diagram for stainless steel weld metal, Metal Progr. 56 (1949) 680–681.
[8] G. Bergman, D.P. Shoemaker, The determination of the crystal structure of the σ phase in the iron-chromium and iron-molybdenum systems, Acta Cryst. 7 (1954) 857–865.
[9] E.C. Bain, W.E. Griffiths, An introduction to the iron-chromium-nickel alloys, Trans. AIME 75 (1927) 166–213.
[10] A.C. Lawson, C.E. Olsen, J.W. Richardson Jr., M.H. Mueller, G.H. Lander, Structure of β-uranium, Acta Cryst. B44 (1988) 89–96.
[11] A.N. Holden, Growth and crystallography of deformation of β-phase uranium single crystals, Acta Cryst. 5 (1952) 182–184.
[12] M.L. Kronberg, Atom movements and dislocation structures for plastic slip in single crystals of β-uranium, J. Nucl. Mater. 1 (1959) 85–95.
[13] C. Rodriguez, J.A. Coll, Deformation mechanisms of β uranium single crystals, J. Nucl. Mater. 11 (1964) 212–219.
[14] M.D. Uchic, D.M. Dimiduk, J.N. Florando, W.D. Nix, Sample dimensions influence strength and crystal plasticity, Science 305 (2004) 986–989.
[15] M.D. Uchic, P.A. Shade, D.M. Dimiduk, Plasticity of micrometer-scale single crystals in compression, Annu. Rev. Mater. Res. 39 (2009) 161–186.
[16] J. Michler, K. Wasmer, S. Meier, F. Östlund, K. Leifer, Plastic deformation of gallium arsenide micropillars under uniaxial compression at room temperature, Appl. Phys. Lett. 90 (2007), 043123.
[17] S. Korte, W.J. Clegg, Discussion of the dependence of the effect of size on the yield stress in hard materials studied by microcompression of MgO, Philos. Mag. 91 (2011) 1150–1162.
[18] N.L. Okamoto, M. Inomoto, H. Adachi, H. Takebayashi, H. Inui, Micropillar compression deformation of single crystals of the intermetallic compound ζ-$FeZn_{13}$, Acta Mater. 65 (2014) 229–239.
[19] S. Korte-Kerzel, Microcompression of brittle and anisotropic crystals: recent advances and current challenges in studying plasticity in hard materials, MRS Comm. 7 (2017) 109–120.
[20] S. Schröders, S. Sandlöbes, C. Birke, M. Loeck, L. Peters, C. Tromas, S. Korte-Kerzel, Room temperature deformation in Fe_7Mo_6 μ-phase, Int. J. Plastic. 108 (2018) 125–143.
[21] K. Kishida, T. Maruyama, H. Matsunoshita, T. Fukuyama, H. Inui, Micropillar compression deformation of single crystals of Mo_5SiB_2 with the tetragonal $D8_l$ structure, Acta Mater. 159 (2018) 416–428.
[22] H. Inui, N.L. Okamoto, S. Yamaguchi, Crystal structures and mechanical properties of Fe-Zn intermetallic compounds formed in the coating layer of galvannealed steels, ISIJ Int. 58 (2018) 1550–1561.
[23] K. Kishida, Y. Shinkai, H. Inui, Room temperature deformation of 6*H*-SiC single crystals investigated by micropillar compression, Acta Mater. 187 (2020) 19–28.
[24] K. Kishida, T. Fukuyama, T. Maruyama, Room temperature deformation of single crystals of Ti_5Si_3 with the hexagonal $D8_8$ structure investigated by micropillar compression tests, Sci. Rep. 10 (2020) 17983.
[25] Y. Hashizume, M. Inomoto, H. Takebayashi, N.L. Okamoto, H. Inui, Micropillar compression deformation of single crystals of the intermetallic compound Γ-Fe_4Zn_9, Acta Mater. 199 (2020) 514–522.
[26] K. Kishida, T. Maruyama, T. Fukuyama, H. Inui, Micropillar compression deformation of single crystals of α-Nb_5Si_3 with the tetragonal $D8_l$ structure, Sci. Tech. Adv. Mater. 21 (2020) 805–816.
[27] Y. Hashizume, M. Inomoto, N.L. Okamoto, H. Inui, Plastic deformation of single crystals of the δ_{1p} and δ_{1k} intermetallic compounds in the Fe-Zn system by micropillar compression, Int. J. Plastic. 136 (2021), 102889.
[28] K. Kishida, M. Okutani, H. Inui, Room-temperature deformation of single crystals of transition-metal disilicides ($TMSi_2$) with the $C11_b$ (TM = Mo) and C40 (TM=V, Cr, Nb and Ta) structures investigated by micropillar compression, Acta Mater. 223 (2022), 117468.
[29] K. Kishida, M. Okutani, H. Inui, Direct observation of zonal dislocation in complex materials, Acta Mater. 228 (2022), 117756.
[30] H.L. Yakel, Atom distributions in sigma phases. I. Fe and Cr atom distributions in a binary sigma phase equilibrated at 1063, 1013 and 923 K, Acta Cryst. B39 (1983) 20–28.
[31] X. Deng, J. Bitler, K.K. Chawla, B.R. Patterson, Toughness measurement of cemented carbides with chevron-notched three-point bend test, Adv. Eng. Mater. 12 (2010) 948–952.
[32] M.G. Mueller, V. Pejchal, G. Žagar, A. Singh, M. Cantoni, A. Mortensen, Fracture toughness testing of nanocrystalline alumina and fused quartz using chevron-notched microbeams, Acta Mater. 86 (2015) 385–395.
[33] Y.Le Page, P. Saxe, Symmetry-general least-squares extraction of elastic data for strained materials from ab initio calculations of stress, Phys. Rev. B 65 (2002), 104104.
[34] G. Kresse, J. Furthmüller, Efficient iterative schemes for *ab initio* total-energy calculations using a plane-wave basis set, Phys. Rev. B 54 (1996) 11169–11186.
[35] J. Havránková, J. Vřešťál, L.G. Wang, M. Šob, *Ab initio* analysis of energetics of σ-phase formation in Cr-based systems, Phys. Rev. B 63 (2001), 174104.
[36] J.P. Perdew, K. Burke, M. Ernzerhof, Generalized gradient approximation made simple, Phys. Rev. Lett. 77 (1996) 3865–3868.
[37] H.J. Monkhost, J.D. Pack, Special points for Brillouin-zone integrations, Phys. Rev. B 13 (1976) 5188–5192.
[38] D.A. Read, E.H. Thomas, J.B. Forsythe, Evidence of itinerant electron ferromagnetism in sigma phase alloys, J. Phys. Chem. Solids 29 (1968) 1569–1572.
[39] J. Cieślak, M. Reissner, W. Steiner, S.M. Dubiel, On the magnetism of the σ-phase Fe-Cr alloys, Phys, Stat. Sol. (a) 205 (2008) 1794–1799.
[40] V. Vitek, Intrinsic stacking faults in body-centered cubic crystals, Philos. Mag. 18 (1968) 773–786.
[41] V. Vitek, V. Paidar, Chapter 87, Non-planar dislocation cores: a ubiquitous phenomenon affecting mechanical properties of crystalline materials, in: J. P. Hirth (Ed.), Dislocations in Solids, Vol. 14, Elsevier, Amsterdam, 2008, pp. 441-514.
[42] A.S. Schneider, D. Kaufmann, B.G. Clark, C.P. Frick, P.A. Gruber, R. Mönig, O. Kraft, E. Arzt, Correlation between critical temperature and strength of small-scale bcc pillars, Phys. Rev. Lett. 103 (2009), 105501-1-4.
[43] D.M. Dimiduk, M.D. Uchic, T.A. Parthasarathy, Size-affected single-slip behavior of pure nickel microcrystals, Acta Mater. 53 (2005) 4065–4077.
[44] H. Bei, S. Shim, G.M. Pharr, E.P. George, Effects of pre-strain on the compressive stress-strain response of Mo-alloy single-crystal micropillars, Acta Mater. 56 (2008) 4762–4770.
[45] S.W. Lee, W.D. Nix, Size dependence of the yield strength of fcc and bcc metallic micropillars with diameters of a few micrometers, Philos. Mag. 92 (2012) 1238–1260.
[46] M.F. Ashby, S.D. Hallam, The failure of brittle solids containing small cracks under compressive stress states, Acta Metall. 34 (1986) 497–510.
[47] C.G. Sammis, M.F. Ashby, The failure of brittle porous solids under compressive stress states, Acta Metall. 34 (1986) 511–526.
[48] M.F. Ashby, C.G. Sammis, The damage mechanics of brittle solids in compression, Pure Appl. Geophys. 133 (1990) 489–521.